Internal tides off the Amazon shelf in the western tropical Atlantic: Analysis of SWOT Cal/Val Mission Data

Michel Tchilibou[1], Loren Carrere[1], Florent Lyard[2], Clément Ubelmann[3], Gérald Dibarboure[4] , Edward D. Zaron[5], and Brian K. Arbic[6]

[1] Collecte Localisation Satellites, 31520 Ramonville-Saint-Agne, France

[2] Université de Toulouse, LEGOS (CNES/CNRS/IRD/UT3), 31400 Toulouse, France

[3] Datlas, Grenoble, France

[4] Centre National d'Etude Spatiales, 31400, Toulouse, France

[5] College of Earth, Ocean and Atmospheric Science, Oregon State University, Corvallis, OR, USA

[6] Department of Earth and Environmental Sciences, University of Michigan, Ann Arbor, MI, USA

Correspondence to: Michel Tchilibou (mtchilibou@groupcls.com)

Abstract

This study focuses on the internal tides (IT) off the Amazon shelf in the tropical Atlantic. It is based on 2 km horizontally gridded observations along the swaths of SWOT (Surface Water and Ocean Topography) track 20 during the calibration/validation phase (Cal/Val, 1-day orbit) from late March to early July 2023. We evaluate the amplitude of M_2, N_2 and S_2 frequencies and use the M_2 atlas as an internal tide correction model for SWOT observations. Internal tide amplitudes (models or atlases) are first derived by harmonic analysis of the SWOT sea level anomaly (SLA). The estimation is improved by performing a principal component analysis (PCA) before the harmonic analysis. The results compare very well with the high-resolution empirical tide (HRET) internal tide model, the reference product for internal tide corrections in altimetry observations. The coherent mode 1 and mode 2 M_2 tides can be distinguished in the internal tide model derived from SWOT, while the higher modes with their strong SLA signature are seen mostly in the incoherent part. In comparison to HRET, the correction of SWOT observations with SWOT-based atlases may be more relevant for this track.

Introduction

The launch of the SWOT mission at the end of 2022 certainly marks a new phase in spatial altimetry. SWOT is equipped with the KaRIn instrument, a Ka-band radar interferometer capable of measuring the sea surface topography with unprecedented resolution in two-dimensional swaths. KaRIn consists of two antennae that take 2D measurements in two 50 km-wide swaths separated by a 20 km gap covered by the conventional nadir radar altimeter also carried by the mission. The accuracy of SWOT's instruments is such that SWOT should be able to observe the ocean down to a spatial scale of 15-30 km (Morrow et al., 2019; Dufau et al., 2016; Wang et al., 2019), thus, complementing our 2D view of the ocean with Topex/Poseidon class nadir altimetry, which is limited to scales larger than 150 km (Chelton et al., 2011; Ballarotta et al., 2019) along one-dimensional tracks rather than two-dimensional swaths. The main oceanographic objective of the SWOT mission is to characterize mesoscale and sub-mesoscale ocean circulation (Fu et al., 2012; Fu and Ubelmann, 2014). However, ocean processes at the scales targeted by SWOT (150-15 km) encompass both "balanced" geostrophic motions, as well as surface and internal inertia-gravity waves at tidal frequencies. The correction of internal tides (IT) surface signatures presents a significant challenge to the useability of SWOT data, considering that the

spatial scales of these waves overlap with those of balanced motions. Conversely, the exploitation of SWOT data to study IT is an opportunity for learning more about these waves and quantifying their impacts in the ocean.

Efforts have been made in recent years to map internal tides using conventional altimetry observations. This was made possible by the fact that the internal tide has a SSH (Sea Surface height) signature of the order of one to several centimeters (Ray and Mitchum, 1997). However, the coarse sampling in both space and time of conventional altimetry is a hindrance. To derive spatially continuous high-resolution maps of the internal tide SSH from the sparse altimeter sampling, Dushaw (2015), Zhao et al. (2019) and Zaron (2019) used least-squares techniques to fit kinematic wave solutions to nadir altimetry. Ubelmann et al., (2022) proposed jointly estimating internal tides and mesoscale eddies to produce 2D maps of internal tides from conventional altimetry observations. The advent of SWOT presents an opportunity to validate these internal tide maps using direct 2D observations of the ocean. However, there is still some debate about the extraction of the internal tidal signal along SWOT swaths. The first objective of our study is thus to estimate the internal tidal signal along the SWOT swaths. Le Guillou et al., (2021) propose a data assimilation method coupled with a simple dynamical model to separate internal tides and balanced motion in SWOT data. The possibility of using deep learning to access internal tide signals is raised by Wang et al. (2022). Without questioning these methods, we will show that classical methods of harmonic analysis and principal component analysis (PCA) can be used to obtain internal tide maps from SWOT data.

Following the linear theory of ocean vertical modes, internal tides can be decomposed as a sum of orthogonal baroclinic modes (Gill, 1982; Kelly et al., 2016). The first modes (mode 1 and mode 2) propagate over hundreds or even thousands of kilometers. Higher modes have much shorter wavelengths and are likely to dissipate close to the internal tide generation site, due to their low group velocity and high shear (St Laurent and Garrett, 2002; Vic et al.,2019) and therefore could barely be observed in classical nadir altimetry observations. In practice, the internal tide is separated into the so-called coherent and incoherent internal tides. The coherent internal tide is the part of the internal tide which remains phase-locked with the generating barotropic tide over an arbitrary period and is easily obtained by harmonic analysis over the targeted period. Consequently, the residual that escapes harmonic analysis constitutes the incoherent internal tide. The amplitude, phase, and trajectory of incoherent internal tide results from refraction, reflection, and advection of internal tide by the ocean background circulation including eddies, currents, and stratification (Ponte and Klein, 2015; Nelson et al.,2019; Buijsman et al., 2017; Dunphy et al., 2017; Dunphy and Lamb, 2014; Duda et al., 2018; Savage et al., 2020; Barbot et al., 2021). The incoherency of the internal tide makes it difficult to correct for in altimetry observations. In the SWOT data processing protocol (Dibarboure et al.,2024), the coherent part of the internal tide is corrected using the HRET (High-Resolution Empirical Tide) model of Zaron (2019). The second objective of this study thus concerns the correction of the coherent internal tide in the SWOT data: between HRET (the reference model) and the internal tide estimates directly on SWOT, which is most relevant for correcting the internal tide on SWOT data?

Like the barotropic tides, the internal tides are a mixture of long- and short-period waves, among which are the main astronomical tides, such as the diurnal waves (O1, K1, P1) and the semi-diurnal waves (M2, S2, N2, K2). Due to the long repeat cycles of altimetry satellites, short tidal periods are aliased to longer periods (Le Provost, 2001). The M2 tide, for example, is aliased to 62.11 days for the TOPEX/Jason 10-day orbit (9.92 days precisely). With SWOT sampling, M2 is aliased to 66.02 days or 12.35 days (Table 1), depending on whether we consider the 21-day final science orbit or the 1-day calibration/validation (Cal/Val) orbit (0.99343 days exactly). Table 1 gives an overview of the aliasing periods of the main diurnal and semi-diurnal tidal frequencies on the SWOT Cal/Val orbit. Table 1 is

completed by the Rayleigh criterion values which provide information on the duration of the records needed to separate the different waves. SWOT was maintained in its Cal/Val orbit for about 6 months, providing slightly more than 3 months of usable data from March to early July 2023. Our study is based on this unprecedented 1-day orbit database and concerns observations along a single SWOT track in the Atlantic Ocean.

Table 1: Period of aliasing (in days, second line) and separability following the Rayleigh criterion (in days, from the third line to the end) of main tidal waves for SWOT's 1-day orbit.

	M2	S2	N2	K2	O1	P1	K1	Sa	Ssa
Periods	12.35	75.60	8.53	129.01	12.97	106.94	258.03	365.26	182.62
M2	--------	14.77	27.55	13.66	258.03	13.97	12.97	12.79	13.25
S2	--------	----------	9.61	182.62	15.66	258.03	106.94	95.34	129.01
N2	-------	-------	--------	9.13	24.9	9.27	8.82	8.73	8.95
K2	--------	-------	--------	--------	14.42	624.89	258.03	199.47	439.51
O1	-------	--------	--------	-------	---------	14.77	13.66	13.45	13.97
P1	-------	--------	--------	-------	--------	---------	182.62	151.20	258.03
K1	-------	--------	--------	-------	------	--------	---------	878.92	624.89
Sa	--------	--------	--------	------	--------	-------	-----	----------	365.22

This study focuses on the Cal/Val track 20 off the Amazon shelf in the western tropical Atlantic between 2°S and 15°N (Figure 1). The track has been chosen because the Amazon shelf is one of the hot spots for internal tide generation in the ocean (Arbic et al., 2012; Solano et al. 2023; Niwa and Hibiya et al., 2011). The region is marked by strong seasonal cycles of stratification, circulation and eddies that regulate the generation and propagation of internal tides (Barbot 2021, Tchilibou et al., 2022). The stratification is modulated by freshwater inflows from precipitation (under the inter-tropical convergence zone) and rivers (Amazon and Para rivers). The strong western boundary current, the North Brazil Current (NBC), controls the extension of the Amazon's plume and develops a double retroflexion into the Equatorial UnderCurrent (EUC, around 2°S-2°N) and the North Equatorial CounterCurrent (NECC, around 5°N-8°N). The barotropic and baroclinic instabilities of these currents generate some of the eddies present in the region (Aguedjou et al., 2019). Internal tides generated between the isobaths 100 and 2000 m along the shelf break propagate mainly from the six sites indicated in Figure 1 (Tchilibou et al.,2022; Assene et al., 2024). Between March and July, the pycnocline is shallow, the mesoscale activity and currents are low, consequently, internal tides tend to keep more coherent (Tchilibou et al., 2022). During the rest of the year, the pycnocline is deeper, mesoscale and currents are strong, and, consequently, the incoherence of internal tides increases as their reflection and advection by the circulation intensifies. As they evolve, internal tides disintegrate into nonlinear internal solitary waves (Jackson et al., 2012; Alford et al., 2015; Egbert and Erofeeva 2021). Packets of nonlinear internal solitary waves (ISWs) have been reported along the Amazon continental shelf and offshore (Lentini et al., 2016; Bai et al., 2021, Brandt et al., 2002; Magalhães et al., 2016). They are highly active in the area (4-8°N /40-45°W, see Figure 2 of de Macedo et al., 2023) of concentration of internal tides rays emanating from sites A and D, and they have a seasonal cycle of occurrence and wavelengths in agreement with those of internal waves (de Macedo et al., 2023).

The orientation of SWOT track 20 in this part of the ocean is such that it intersects three areas with potentially different dynamics (Tchilibou et al., 2022). Between 2.5°S and 2.5°N (area 1, Figure 1), the track is in the path of internal tides generated at points B, C and, to a lesser extent, A. In area 2, between 2.5°N and 8°N (Figure 1), the track crosses the zone of interaction between internal tides and mesoscale. Finally, area 3, north of 10°N (Figure 1), lies on the mid-Atlantic Ridge, where some IT can likely be generated also. We will keep all this in mind when interpreting our results.

124   The paper is structured as follows: The data used, the evidence for the presence of internal tides in
125   the SWOT data and the variability of the SLA at different scales are presented in section 1. The
126   amplitude of the internal tides is first estimated from the SWOT data in section 2. In section 3, the
127   estimation of internal tides is improved by introducing PCA. The SWOT based internal tide models and
128   HRET are further compared in section 4. The paper ends with a conclusion and discussion.

129
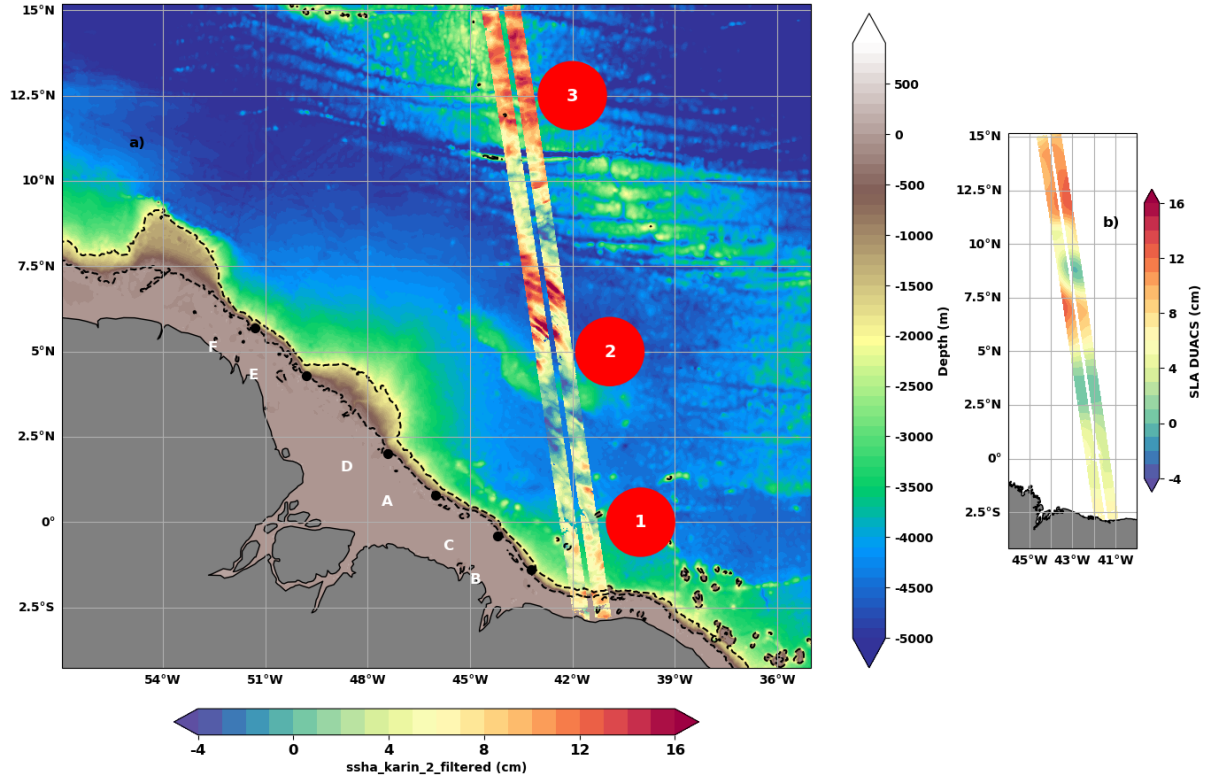
Figure 1: a) Bathymetry (m) off the Amazon shelf in the western tropical Atlantic. SLA KaRin (cm) on
08 April, 2023, along track 20 of SWOT's 1-day cycle. The main internal tide generation sites are marked
by the letters A to F. The 200 and 2000 m isobaths are dotted. The circles locate area 1 (2.5°S to 2.5°N),
area 2 (2.5°N to 8°N) and area 3 (north of 10°N) along the track. b) large scale structure from DUACS
at the same date.

1- Data and Variability: Evidence of IT propagation at different scales

1.1- Description of the database:

137   We use version V0.3 of the L3 SWOT products, released in December 2023. The data, made up of
138   several variables, are provided on regular horizontal grids of 2 km by 2 km. Using the naming
139   convention used in the dataset, we have defined the SLA by equation 1 below:

140   SLA = ssha_karin_2_filtered+ internal_tide_hret - duacs_ssha_karin_2_oi,   (1)

141   The first term on the right, 'ssha_karin_2_filtered' (the same as ssha_noiseless), is the SWOT
142   observation at the two KaRIn swaths only. We exclude SWOT nadir observations, to focus on the
143   SWOT's potential to observe directly 2D maps of the ocean. The ssha_karin_2_filtered has been
144   denoised using data-driven machine-learning noise reduction and corrected from all the classic
145   physical, instrumental and environmental corrections applied in altimetry (Dibarboure et al. 2024). The
146   tidal corrections applied are FES2022 model (Lyard et al., personal communication; Lyard et al., 2021)

147 for the barotropic tide and HRET for the internal tide (Zaron, 2019). We reintroduced HRET's internal
148 tide SSH (internal_tide_hret), so that our final SLA contains the total internal tide signal. The last term
149 'duacs_ssha_karin_2_oi' corresponds to the DUACS Maps of Sea Level Anomaly (MSLA) interpolated
150 on SWOT swaths (Ballarotta et al., 2023; Ubelmann et al. 2015, 2021). It removes the large-scale ocean
151 signals and particularly the mesoscale eddies that can mask internal waves at these latitudes. On track
152 20, we have the SLA from March 29 to July 10, 2023, i.e. 104 cycles with completely or partially filled
153 swaths. We have removed the mean SLA from the entire Cal/Val mission.

154   We recall that HRET is an empirical estimate of the internal tides at the M2, S2, K1 and O1
155 frequencies. The variable internal_tide_hret in the SWOT data and HRET model in this paper refers to
156 the HRETv8.1 version (Zaron, 2019). This version was developed by analyzing 25 years (1993-2017) of
157 exact-repeat mission altimetry including the TOPEX/Poseidon-Jason missions, the ERS-Envisat-AltiKa
158 missions and the GEOSAT Follow-On mission. The implementation of HRET involves a local two-
159 dimensional Fourier analysis of the along-track data, and the determination of the coefficients of a
160 spatial model by weighted least-squares fitting (second order polynomials fitting). The estimated tidal
161 fields are gridded on a regular latitude-longitude grid by weighted averaging, and a mask is used to set
162 the values to zero in regions where the estimate is too noisy. HRET includes mode 1 and mode 2
163 internal tides, but mode 2 is very weak in the present study area.

164 **1.2- Evidence of IT propagation at different scales:**

165   The snapshots in Figure 2a show very fine-scale crest-like structures superimposed on positive and
166 negative SLA spaced tens and hundreds of kilometers apart. The scenario repeats itself on the other
167 cycles (see movie in the supplementary material), indicating that SWOT likely sees internal waves of
168 different spatial scales. We submitted the SLA to spectral analysis to learn more about its frequency
169 and wavelength. The 2D FFT spectra are computed in the time (cycles) and along-track (latitude)
170 dimensions and then averaged over the cross-track (longitude) dimension. The Tukey 0.25 window is
171 used for windowing. The wavenumber-frequency (Figure 3a) was integrated to derive the
172 wavenumber spectrum (Figure 3b) and the frequency spectrum (Figure 3c).

173
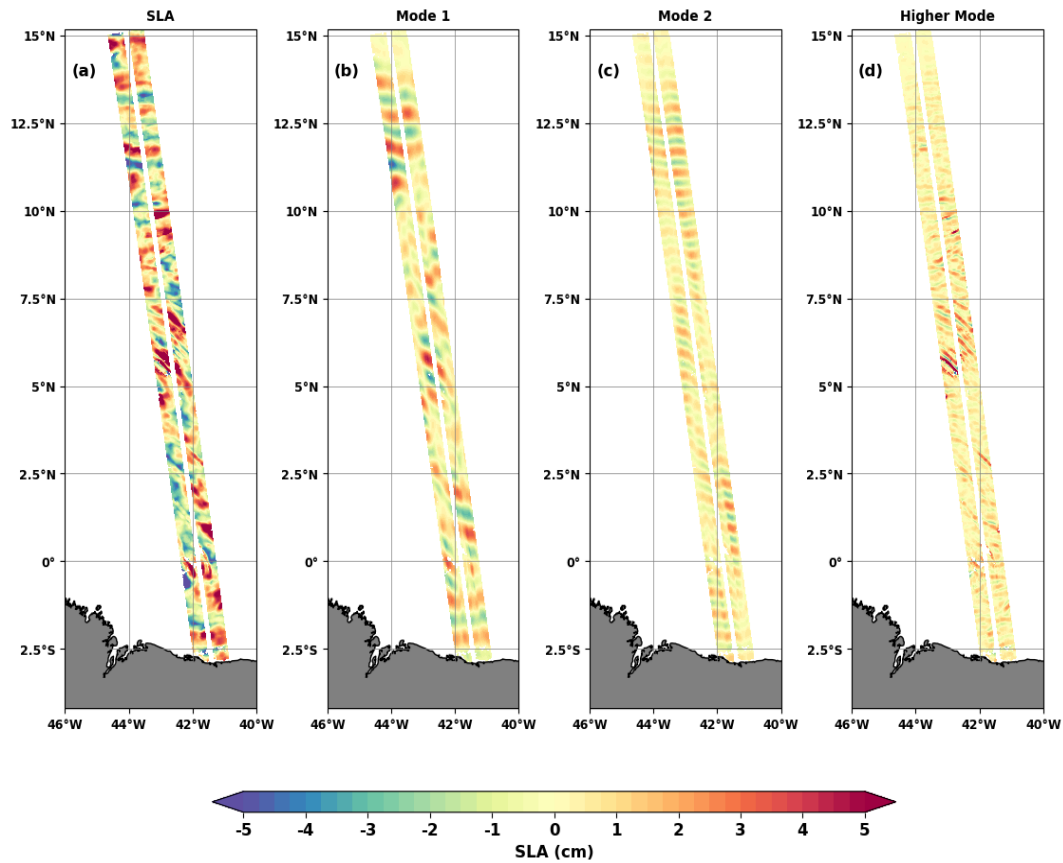
Figure 2: Snapshot of SWOT SLA on April 8, 2023. a) Total SLA, b) Mode 1 FFT-filtered SLA (180-90 km), c) Mode 2 FFT-filtered SLA (80-60 km) and d) Higher mode FFT-filtered SLA (50-2 km).

176

The wavenumber-frequency (Figure 3a), the wavenumber (Figure 3b) and the frequency (Figure 3c) spectra of SWOT SLA indicate that the dominant signal is M2 aliased to 12.22 days (see Table 1). At the M2 aliased frequency, the energy is greatest between 180-90 km and between 80-60 km (Figure 3a), leading to the spectral peaks in Figure 3b. These two wavelength bands correspond well to the theoretical baroclinic mode 1 and 2 scales expected for the internal tide in this region (Zhao, 2021). We isolated the SLA for these two wavelength bands using FFT filtering. When filtering, the FFT is calculated on the along-track dimension. Snapshots of the Mode 1 and Mode 2 SLA are shown in Figures 2b and 2c for the same day as Figure 2a, revealing more of the SLA's wave-like behavior.

Figure 2d shows the FFT-filtered SLA between 50-2km. This band contains all the small-scale structures, including the very remarkable and intense one that appears as wave crests on the SLA. On the wavenumber-frequency spectrum (Figure 3a), the energy maximum at frequency M2 extends to scales smaller than 50 km. According to Barbot et al., (2021), this could be associated to internal tide of mode 3, mode 4 and mode 5. We therefore consider the 50-2 km band as consisting of higher modes.

191

192
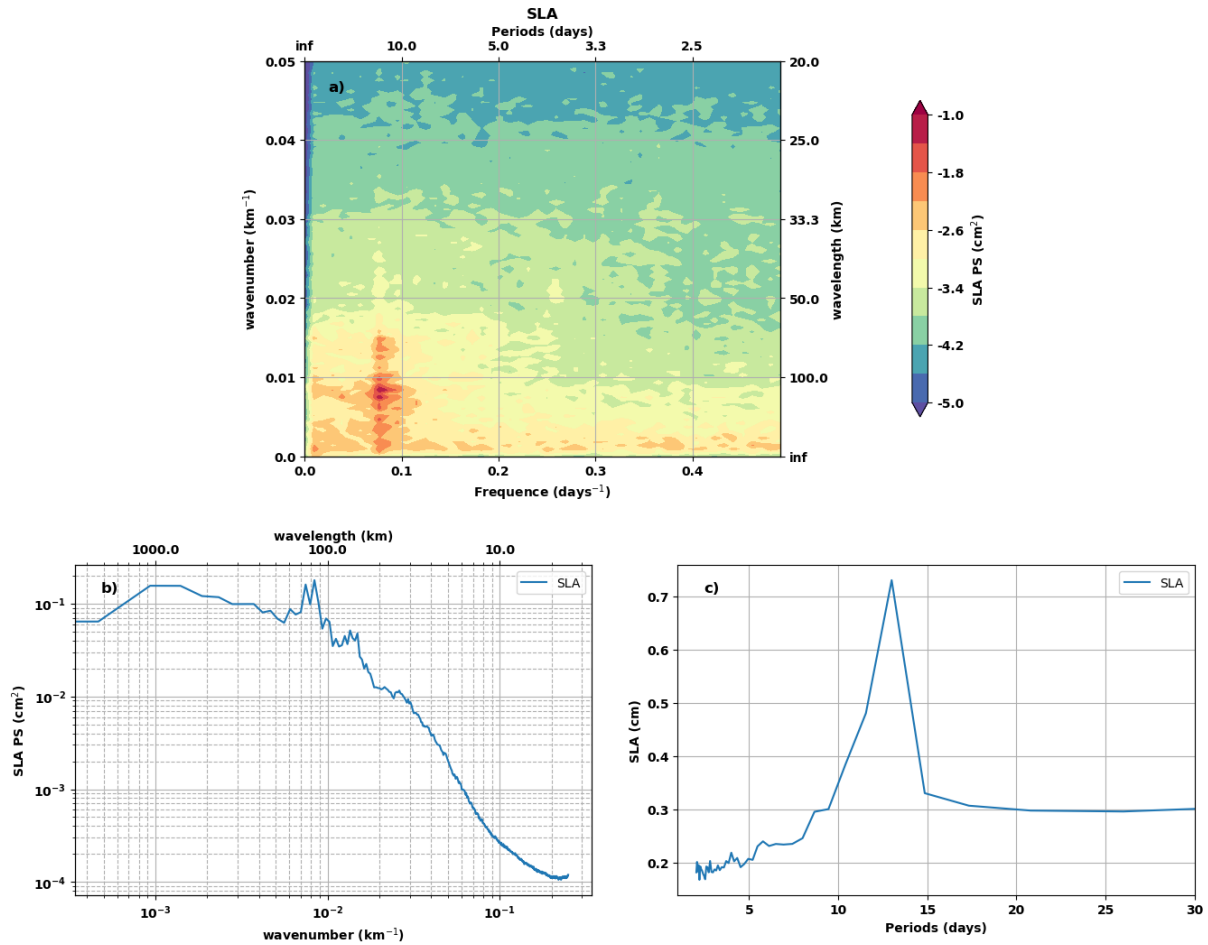
Figure 3: Wavenumber-frequency (a), wavenumber (c) and frequency (d) spectra of the total SLA.

1.3- Variability analysis of IT observations:

Analyses of SLA variability are completed by calculating the standard deviations of the total and the spatially FFT-filtered SLAs in the wavelength bands defined above. Over the Cal/Val period, SLA varies between 1 and 5 cm under track 20 (Figure 4a). Apart from the area very close to the coastline, there are three main patches of maximum variability, each located in one of the dynamic areas highlighted in the introduction. The maximum variability of the SLA in area 1 (2.5°S-2.5°N) is mainly due to the regular mode 1 internal tide flux likely coming from sites A, B and C (Figure 4b). Mode 2 and higher modes contributions are secondary (Figures 4c and 4d) in area 1. Higher modes have a major impact on the variability in area 2 where they make the SLA vary by 2 to 3 cm (Figure 4d), i.e. almost of the same order as mode 1 in the same area. As area 2 is far from the generation sites of the Amazonian shelf-break, the higher modes here are likely to originate from desintegration of mode 1 and mode 2. In area 3, SLA variability is driven mainly by mode 1 and mode 2.
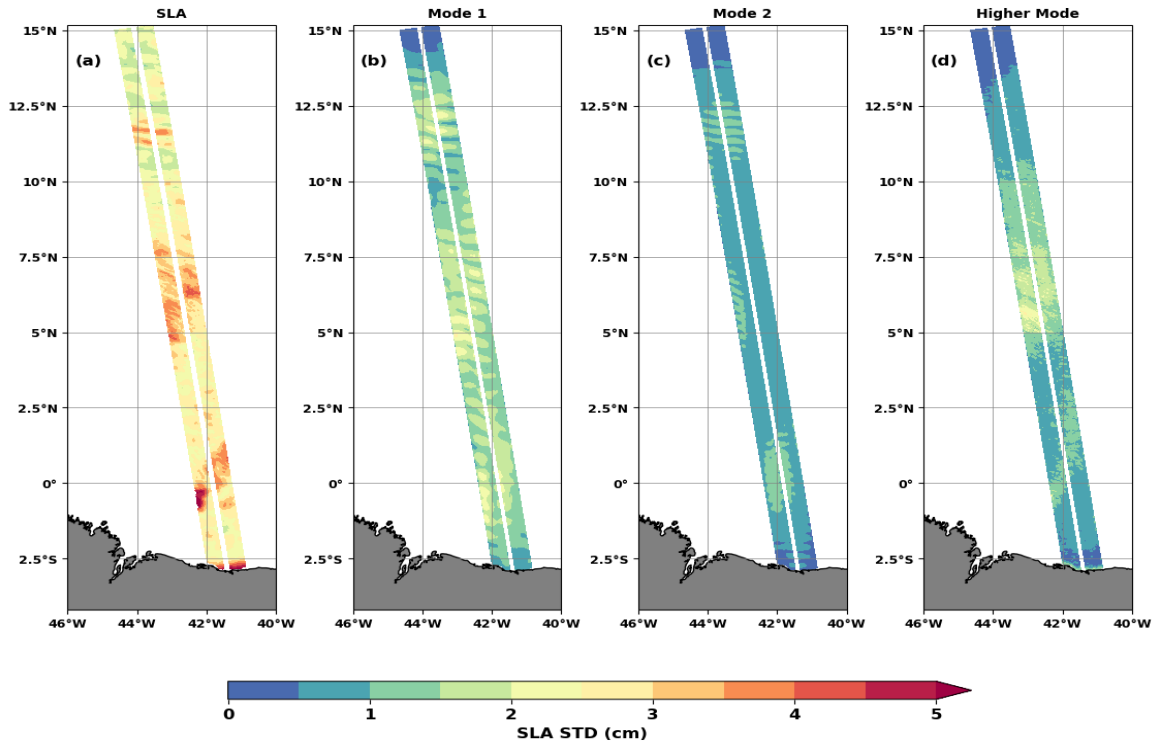
Figure 4: Standard deviation (in cm) of the total (a) SLA, and mode 1(b), mode 2 (c) and higher mode (d) FFT-filtered SLA.

2- The M2, S2 and N2 coherent internal tides from SWOT: ITkars model

In Table 1, 4 waves (M2, N2, S2, and O1) have aliasing periods shorter than the 104 days corresponding to the total length of our SWOT SLA series and are a priori of interest for our analysis. But given the Rayleigh criterion between them in Table 1, it is reasonable to restrict ourselves to the three semi-diurnal waves. Harmonic analysis based on least-squares fitting is used to extract the coherent internal tide at each band point with at least 80 valid cycles over the entire SWOT Cal/Val observation period. In the following, ITkars (IT from KARin Swot) refer to SWOT estimation of IT.
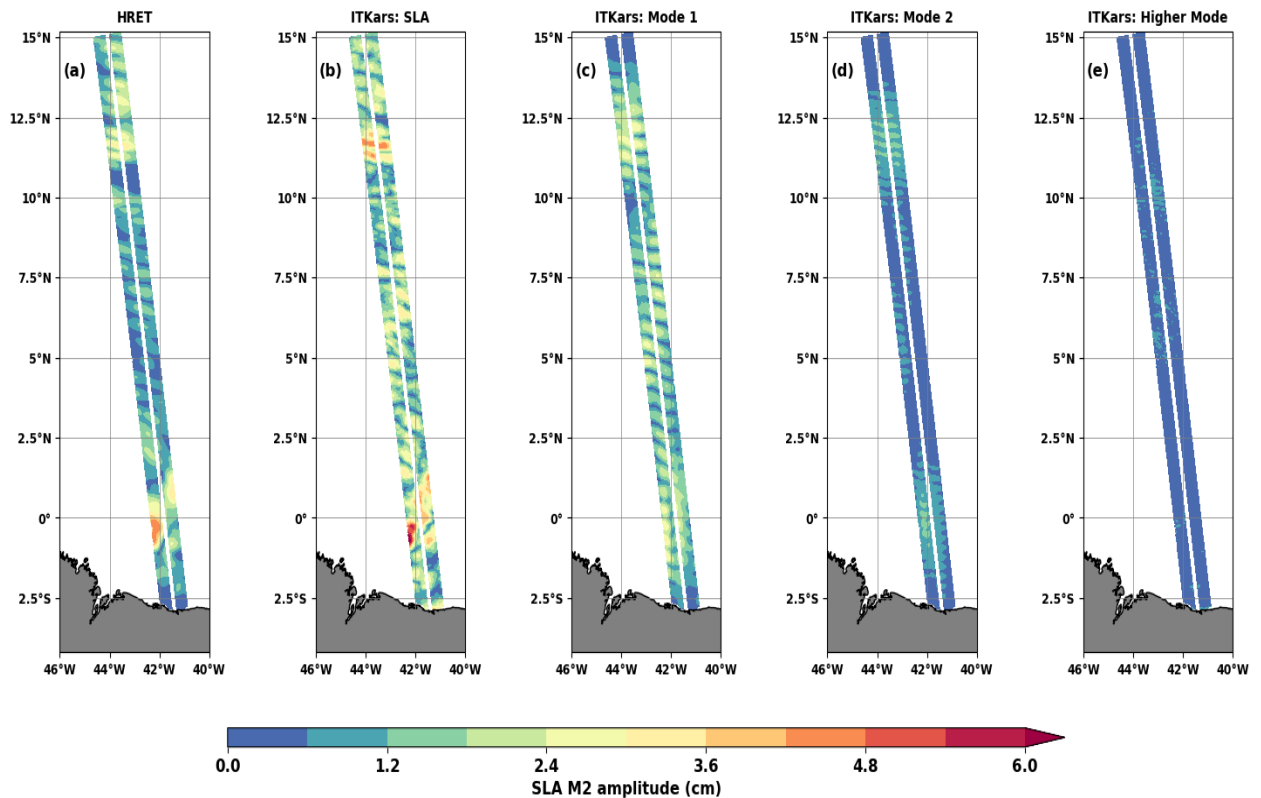
Figure 5: The amplitude (in cm) of the M2 internal tide from the HRET model (a) and the ITkars (b to e) model over the cal/val period. ITkars is derived by harmonic analysis of the total SWOT SLA (b) and FFT-filtered SWOT SLA for mode 1 (c), mode 2 (d) and higher mode (e) SLA. Only swath points with at least 80 valid cycles were analyzed.

The amplitudes of the coherent internal tide at the M2 frequency are presented in Figure 5 for both HRET (which include mostly mode 1 on this area) and ITkars models (which include mode 1 and mode 2). We first performed the harmonic analysis of the total SLA (Figure 5b) and repeated the harmonic analyses for each of the FFT-filtered SLAs (Figure 5c to e). The HRET model (Figure 5a) and the ITkars model based on the total SLA (Figure 5b) are similar in terms of spatial distribution, but as expected HRET has smoother and lower amplitudes because it represents a mean on many years of altimetry data. In areas 1 and 3, ITkars shows spatial features identical to those already observed on the standard deviation in Figure 4a. So, the maximum variability for these two parts of the SWOT track is indeed due to the M2 coherent internal tide. The discrepancies between standard deviations (Figure 4) and internal tide amplitudes (Figure 5) are best seen by directly comparing the maps for the different modes or wavelength bands. In area 2, the amplitude of the coherent internal tide is less than 1.5 cm for the higher modes (Figure 5e), whereas at these scales the standard deviation is maximal (Figure 4d). The high variability of the SLA found in area 2 is evidently related to internal tide incoherency.

As S2 from HRET shows unexpected patterns (not shown) and, and N2 is not available in HRET,we show only ITkars results in Figure 6. Both waves have smaller amplitudes than M2 and do not have the same structure as the latter. As the semi-diurnal S2 and N2 IT should have similar patterns to M2, those results indicate that these frequencies are certainly contaminated by other tidal waves due to poor separability on the available period (see Table 1) and are likely also contaminated by the mesoscale. Can we hope to improve our estimate of the coherent internal tide from SWOT observations?
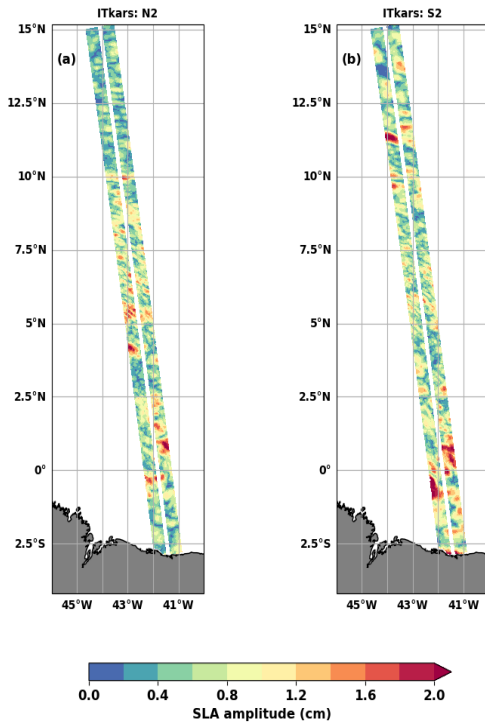
Figure 6: The amplitude (in cm) of the N2 (a) and S2 (b) internal tide of the ITkars model derived by harmonic analysis of the total SLA over the Cal/Val period. Only swath points with at least 80 valid cycles were analyzed.

3- An attempt to improve the estimation of coherent internal tide from SWOT Cal/Val data: Using principal component analysis (PCA) to separate SLA content

3.1- Separation using PCA

PCA, also known as EOF (Empirical Orthogonal Function), is a statistical analysis technique for reducing the dimensionality of a data set (Jolliffe, 1986). Applied to geophysical data, PCA separates the total signal into independent spatial patterns associated with independent temporal components (Principal Component) and gives a measure of the relative importance of each pattern (a percentage of the total variance). The first principal components (PC) capture most of the variance in the data and generally have a repetitive and persistent structure, thus behaving approximately like the stationary component of the signal. In particular, coherent internal tides have significant spatial correlations that PCA could identify and isolate. On this basis, we believe that PCA applied to our total SLA can help better isolate the coherent internal tide (which is stationary) from the remaining residual tidal (incoherent internal tides) and non-tidal signals observed by SWOT. Egbert and Erofeeva (2021) have successfully used PCA to determine the characteristics of the incoherent internal tide around the Amazon shelf. In this paper we focus on the coherent internal tide. Therefore, we performed the PCA on the 104 cycles of the SWOT KaRin total SLA as defined in Equation 1. At each point in the swath, we filled in the missing value with the local time mean, then normalized the time series to ensure that the time mean, and the standard deviation become zero and one respectively. The covariance matrix is calculated on the normalized SLA, the PCA focuses on eigenvalues and not absolute values.

The two leading PCA modes shown in Figure 7 account for 12.3% (PCA1, Figure 7a and c) and 9.1% (PCA2, Figure 7b and d) of the total variance. Their spatial patterns correspond to IT structures: on PCA1 (Figure 7a) the IT is intensified in area 1 and area 3, while PCA2 (Figure 7c) is characterized by an

increase of the IT intensity in area 2. PCs show 12–13 days oscillations with modulations around 70 days (Figure 7b and 7d), therefore recalling the aliasing periods of M2 and S2 waves (see table 1). To get a more precise idea of the wavelengths and frequencies contained in PCA1 and PCA2, we reconstructed the SLA for both components (SLA_pca1 and SLA_pca2) and calculated the spectra shown in Figure 8 (blue line for PCA1 and orange line for PCA2).
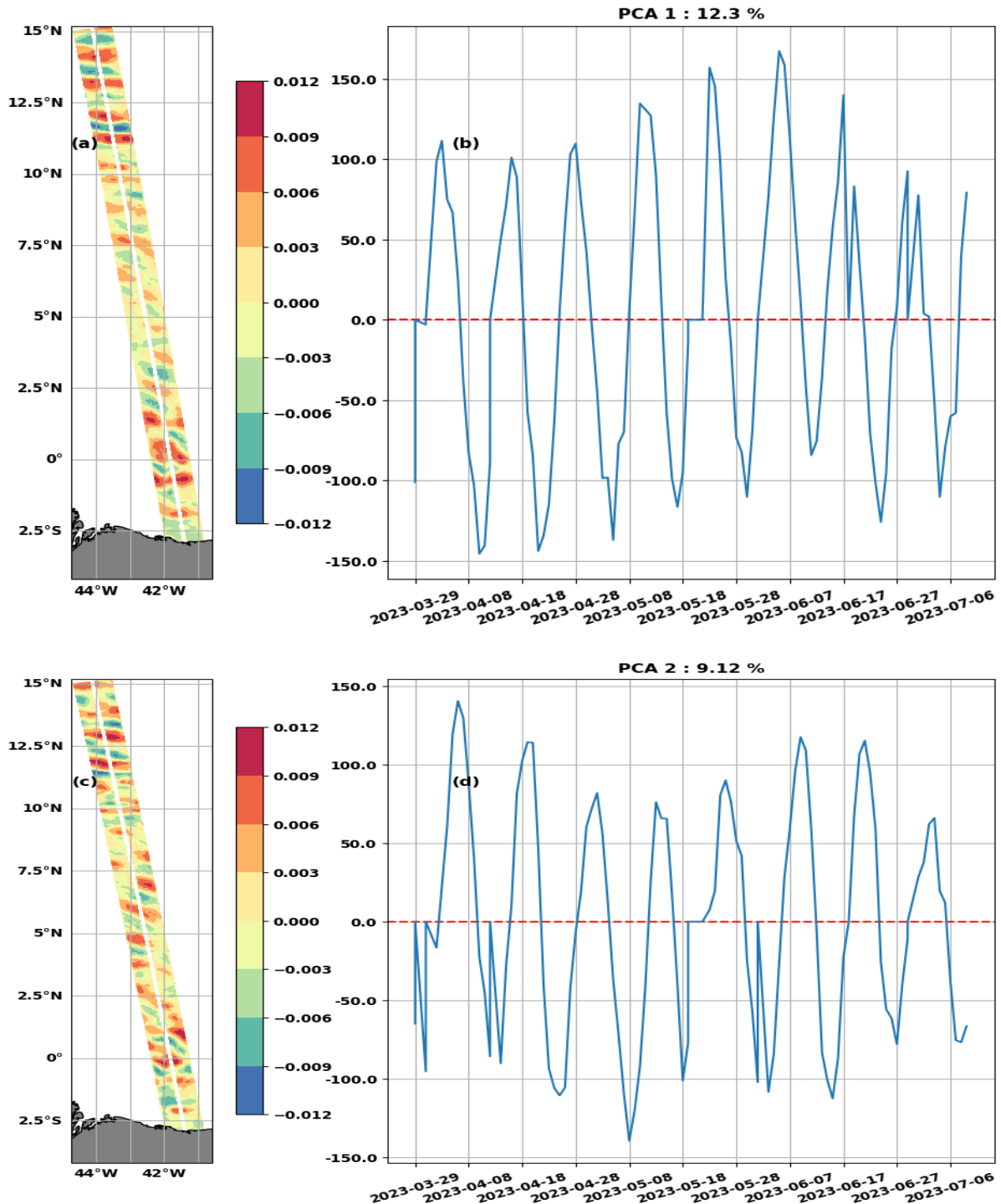
Figure 7: Spatial (left) and principal (right) components of PCA1 (top) and PCA2 (bottom) of the SLA along SWOT swaths over the Cal/Val period.

The wavenumber spectra (Figure 8a) indicate that PCA1 and PCA2 consist mainly of mode 1 (180-90 km) and mode 2 (80-60 km) IT. A peak that could be associated with mode 3 stands out on the PCA2

281 spectrum, but overall, the energy levels of both spectra remain low for higher modes (50-2 km). The
282 frequency spectra (Figure 8b) confirm that M2 is the dominant signal. At this frequency, the mean SLA
283 amplitudes are 0.52 cm for PCA1 and 0.45 cm for PCA2, respectively 71% and 61% of the 0.73 cm
284 associated with the peak of the total SLA reported by the solid black line in Figure 8b. Amplitudes are
285 low for other frequencies. The 104 available cycles are not enough to observe 70-days modulation on
286 the frequency spectra. Given the wavenumber and frequency spectra, we can say that PCA1 and PCA2
287 are two complementary representations of the propagation and evolution of the M2 dominant internal
288 tide, so they can be merged to form a single signal. We have summed SLA_pca1 and SLA_pca2 into
289 SLA_pca_L2 (L2 refers to lower or equal to 2). A snapshot of SLA_pca_L2 is shown in Figure 9a for the
290 same cycle as in Figure 2. Interestingly, the SLA reconstructed with PCA1 and PCA2 have similar
291 patterns to the mode 1 and mode 2 FFT-filtered SLAs (Figures 2b and 2c).

292   Between PCA3 and PCA12 the variance explained is less than 3.5% per PCA, from PCA13 onwards,
293 the variance becomes less than 2% (not shown). The PCs are a mixture of several wave frequencies,
294 with M2 of lower intensity than in PCA1 and PCA2, high frequency (faster than 10 days) and low
295 frequency (15, 17 or even 25 days). It is difficult to associate the spatial patterns of these PCAs with
296 the propagation of a persistent IT in time and along the track, or even with a mode of ocean variability
297 to our knowledge. The last 3 PCA patterns resemble residual noise from the processing of raw SWOT
298 data. We grouped PCA3 to PCA104 into SLA_pca_G2 (G2 for greater than 2). The small-scale structures
299 that were identified in Figure 2a are clearly visible in the snapshot of the SLA_pca_G2 in Figure 9b.
300 Figures 9a and 9b are complementary, as the PCA acted as a filter. The total SLA is now split into
301 SLA_pca_L2 and SLA_pca_G2. The spectra of SLA_pca_G2 are shown in green in Figure 8. Nearly all
302 energies for scales above 180 km (seen as large scale) and below 50 km (for higher modes) are found
303 in the wave number spectrum of SLA_pca_G2. Around the aliased frequency of M2, the mean
304 amplitude is 0.19 cm for SLA_pca_G2. This is about a quarter of the mean amplitude of the total SLA
305 (0.73 cm). With such a drop in the energy of the spectrum, it's tempting to say that separation by the
306 PCA has acted in the same way as a classical detiding. To verify this, we calculated the spectra of the
307 total SLA detided with M2 from ITkars and plotted them as a dashed black line in Figure 8. At all
308 frequencies and wavelengths, they overlap well with the spectra of SLA_pca_G2. Therefore,
309 SLA_pca_G2 is more representative of the incoherent internal tide and SLA_pca_L2 is more suitable
310 for improving the estimation of the coherent internal tide.

311

312

313
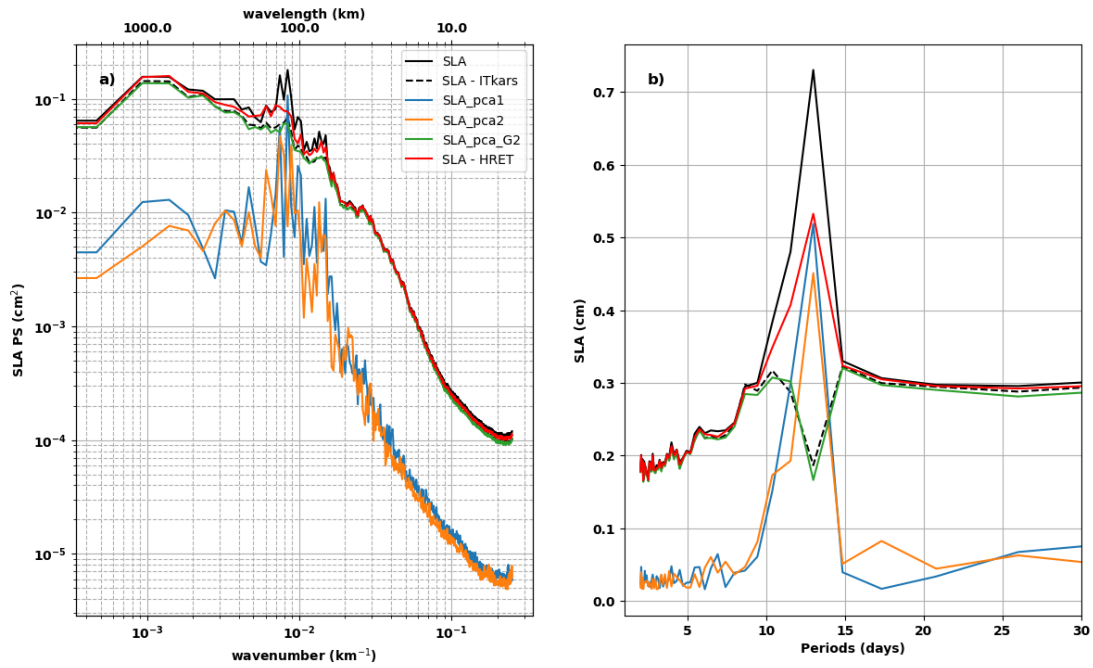
Figure 8: Wavenumber (a) and frequency (b) spectra of SLA_pca1 (in blue), SLA_pca2 (in orange), SLA_pca_G2 (in green), SLA – HRET (in red) and SLA - ITkars (black dashed line). SLA_pca_G2 is the sum of the SLAs of PCAs greater than 2. The spectra of total SLA (black solid line) from Figure 3 are reported here. ITKars is the internal tide model derived from SWOT KaRIn data (cf in section 2).

318
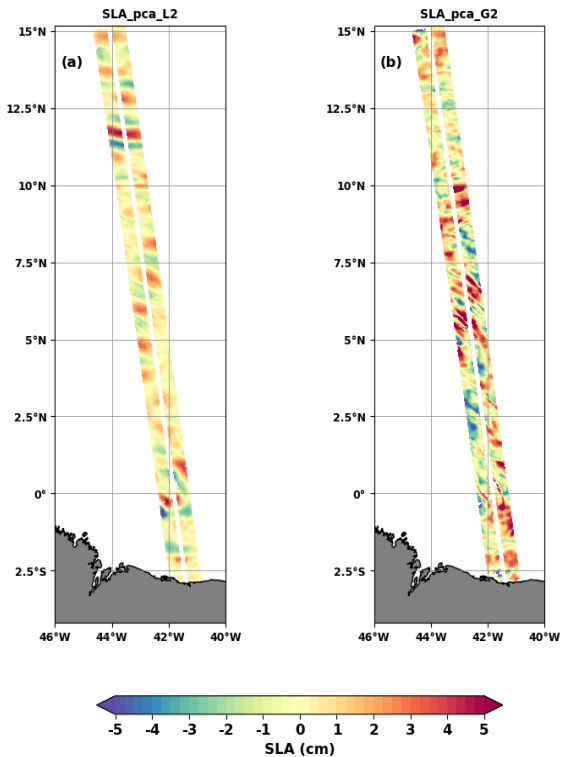
Figure 9: Snapshot of SWOT SLA_pca_L2 (a) and SLA_pca_G2 (b) on 08 April, 2023 (as in Figure 2). SLA_pca_L2 is the sum of the SLAs of PCs less than or equal to 2 (PC1 and PC2).

321

3.2- ITkars_pca internal tide model

323   We have performed the harmonic analysis of SLA_pca_L2 at the semi-diurnal frequencies M2, N2
324   and S2 (Figure 10). The resulting internal tide amplitude (model) is referred to as ITkars_pca to
325   distinguish it from ITkars based solely on harmonic analysis of SWOT Karin data. Compared to Figure
326   6 corresponding to ITkars, the ITkars_pca internal tide maps for N2 (Figure 10a) and S2 (Figure 10b)
327   are cleared of small scales, and the patterns for both waves are now close to that of M2 as expected
328   (Figure 10c and 5b reported in 10f). At first glance, there seems to be no difference between ITkars
329   (Figure 5b or 10f) and ITkars_pca (Figure 10c) for M2. By making the complex difference between the
330   two signals (Figure 10c and 10f), we deduce the amplitude shown in Figure 10d, which is equivalent to
331   the amplitude of the harmonic analysis of SLA_pca_G2 at M2. As with N2 and S2, Figure 10d shows
332   that M2 ITkars (Figure 5b or 10f) also contains an additional signal dominated by small scales, and
333   which does not resemble the classic internal tide.

334

335
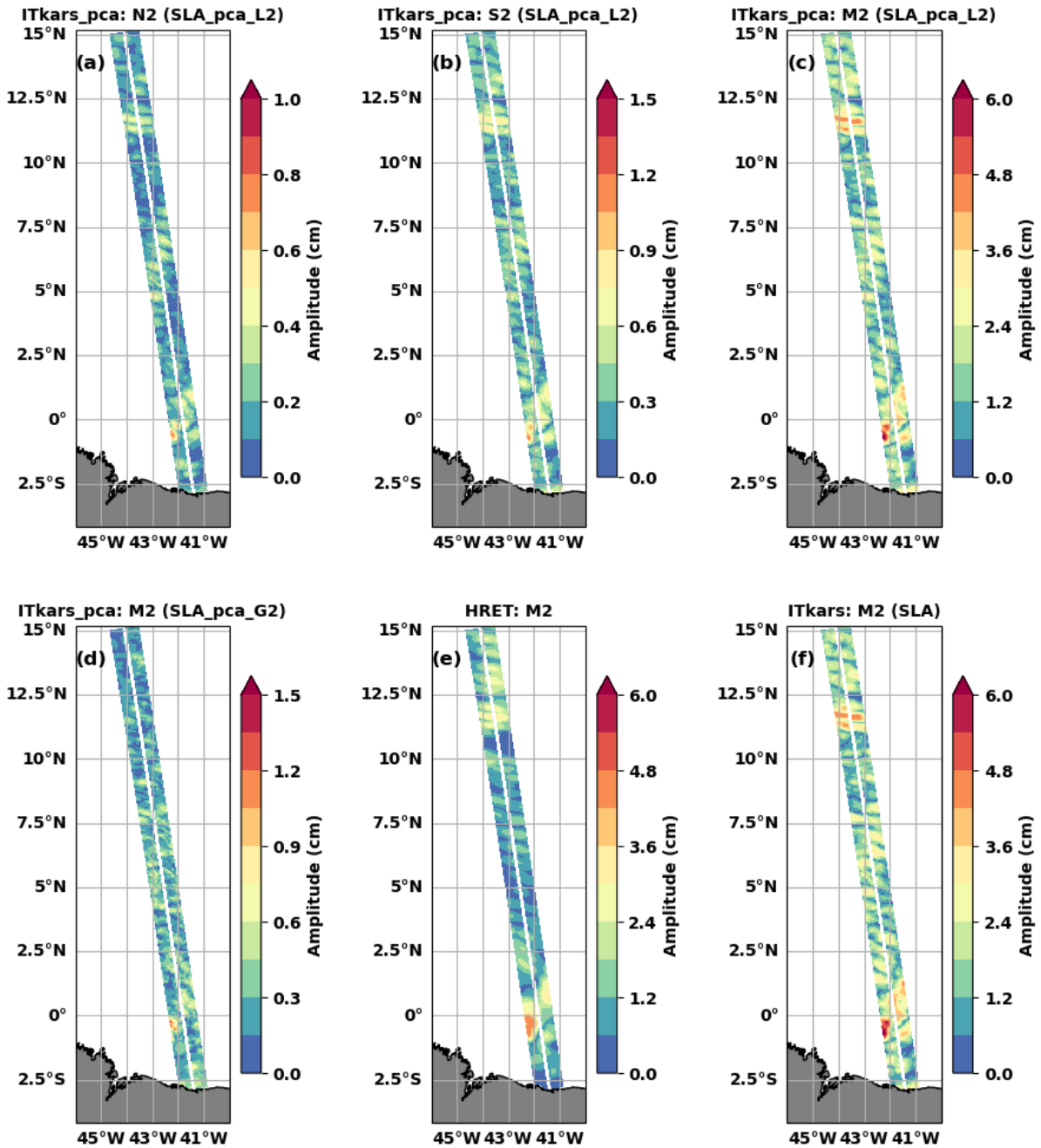
Figure 10: The amplitude (in cm) of the internal tides N2 (a), S2 (b) and M2 (c and d) of the ITkars_pca model derived by harmonic analysis of SLA_pca_L2 (a to c) and SLA_pca_G2 (d) over the Cal/Val period. SLA_pca_L2 is the SLA based on PCA1 and PCA2, SLA_pca_G2 is compiled from PCA3 to PCA104. Only swath points with at least 80 valid cycles were analyzed. Figure 5a and 5b are reported here, M2 HRET (e) and M2 ITkars (f).

The origin of the extra signal contaminating ITkars could be dynamic or numerical. Dynamically, these could be very intense non-linear waves, solitons, or incoherent internal tides, which are retained in the harmonic analysis of section 2 due to the short length of the time series. On the numerical side, noise linked to the pre-processing of SWOT data cannot be ruled out. Another source of contamination could also be the DUACS correction we apply beforehand to distinguish internal tides.

4 - Complementary comparison between SWOT and HRET IT models: predictability of internal tides

348   The comparison between HRET and SWOT based internal tides models (ITkars and ITkars_pca) is
349   taken a step further in this final section. Each of the atlases (amplitude and phase) will be used as an
350   internal tide correction model for the SWOT data. This involves making internal tide predictions over
351   a given period and then subtracting these predictions from raw observations. Various metrics are used
352   to quantify the capability of each model to reduce the variance.

353   In Figure 8, the ITkars M2 atlas has been used as a correction model to detide the total SLA over the
354   entire Cal/Val observation period (black dashed line). We have done the same with M2 from HRET and
355   the corresponding spectra is shown in red in Figure 8. As in figure 3, the 1D spectra are integrations of
356   the 2D wavenumber-frequency spectrum. On the wavenumber spectra, the peaks of modes 1 and 2
357   are reduced but remain visible whatever the detiding applied (Figure 8a). We have integrated the
358   wavenumber spectra of the total SLA (Black line in Figure 8) and the detided SLA (Black dashed and red
359   line in Figure 8) over all wavelengths, between 180 and 90 km for mode 1, between 80 and 60 km for
360   mode 2, from 50 to 2 km for the higher modes, and finally over wavelengths greater than 180 km for
361   the large scale. The derived standard deviations are presented in Table 2 for the total SLA and the SLA
362   detided with ITkars or HRET, as well as the percentages expressing the residual variance rate (ratio of
363   the variances of the detided SLA on the total SLA). The higher is the standard deviation of the detided
364   SLA or the percentage in Table 2, the less efficient is the correction used for detiding. According to
365   Table 2, the application of the M2 internal tide prediction of each of the models removes very little
366   variance from the SLA, nevertheless ITkars is more efficient than HRET especially at mode 1 and mode
367   2 scales. For these scales, the residual variance reaches 76% and 84% of the SLA after correction by
368   ITkars and is likely to be incoherent internal tide. For the higher modes, Table 2 agrees with Figure 5e:
369   the M2 correction has no effect on these scales. ITkars has a greater impact on large scale SLAs than
370   HRET: HRET has almost no signal at large scale by construction, while ITkars can capture some
371   variability at large scales due to short time-series and no fitting approximation.   When detiding with
372   ITkars, the energy spectrum (Figure 8b) decreases strongly around the aliased frequency of M2 (around
373   13 days, see Table 1). The mean of SLA amplitude along the SWOT swaths drops by 74% (from 0.73 cm
374   to 0.19 cm) after ITkars detiding at M2 frequency. With the HRET correction (Figure 8), the peak
375   amplitude at the M2 frequency is 0.53 cm, i.e. a 27% reduction of the peak of the total SLA, which is
376   more than twice lower than with the ITkars correction. It can also be seen that periods of more than
377   15 days and less than 5 days are not affected by the correction, since we have limited ourselves to M2
378   frequency.

379   **Table 2:** Comparative table of the standard deviations of total SLA and SLA detided with HRET or ITkars.
380   Standard deviations are obtained by integrating the spectra of Figure 3c on different wavelength bands
381   (in cm). The ratio between detided SLA and total SLA, computed as a percentage, is given in
382   parentheses.

	All wavelengths	Large scales >180km	Mode 1 180 - 90km	Mode 2 80 - 60km	Higher modes 50 - 2km
Total SLA	1.82	1.07	1.03	0.58	0.74
Detided ITkars	1.6 (88%)	0.99 (93%)	0.78 (76%)	0.49 (84%)	0.71 (96%)
Detided Hret	1.71 (94%)	1.04 (97%)	0.89 (86%)	0.54 (93%)	0.73 (99%)

383

384   The better performance of ITkars correction in comparison to HRET is not surprising, since ITkars is
385   derived from the same database to which the detiding is applied. The result is almost identical to ITkars
386   when the SLA is detided with M2 from ITkars_pca. This is not surprising as the amplitude of the M2

residual in SLA_pca_G2 is small (Figure 10d). To obtain the best possible comparison between ITkars and ITkars_pca still focusing on M2 wave, we propose to apply the detiding to data that are independent of those used to derive the internal tide atlas. Thus, the SWOT data were divided into two periods: period 1, comprising the first 70 cycles (from late March to early June), and period 2 (from early June to early July), comprising the last 34 cycles. We repeated the M2 harmonic analysis of the total SLA over period 1 and derived the atlas "ITkars_p1" (p1 indicates period 1). We did the same with SLA_pca_L2 and derived the atlas "ITkars_pca_p1". The atlases ITkars_p1, ITkars_pca_p1 and HRET are then used to detide the SLA and SLA_pca_L2, first in period 1 and secondly in period 2, which is independent of period 1. Since period 2 is short for frequency spectral analysis, we're going to look at the standard deviation (Table 3) and the variance reduction (Figure 11). Variance reduction is calculated from equation 2 as the difference between the variance of corrected SLA and the variance of the uncorrected SLA (or SLA_pca_L2). A negative variance reduction indicates that the internal tide correction reduces the SLA variance.

$$\text{Variance reduction} = \text{var} (SLA - M2\ \text{atlas}) - \text{var} (SLA) \tag{2}$$

The spatial mean of the standard deviation is summarized in Table 3. On period 1, the standard deviation of the total SLA is 2.56 cm. After correction with M2 of the HRET model, the standard deviation drops by 7% (to 2.39 cm). The SLA standard deviation decreases by about 15% and 14% with ITkars_p1 and ITkars_pca_p1, respectively. The difference between the two ITkars models is not significant as we detide the same data that are used to derive the models (ITkarsp1 in particular). The application of the corrections to SLA_pca_L2 reduces the residual standard deviation from 1.33 cm to 0.99 cm for HRET, to 0.53 cm for ITkars_p1 and to 0.42 cm for ITkars_pca_p1. This shows that even in an SLA dominated by coherent internal tides, HRET removes only 15% of the variance, whereas SWOT-based internal tide models remove over 60%. ITkars_pca_p1 is obviously the best correction for SLA_pca_L2, with ITkars_p1 being slightly less efficient.

On period 2, the corrections of the SLA with the three internal tide models are less efficient. Table 3 shows that, on average, between 5% and 9% of the SLA variance is suppressed, with ITkars_pca_p1 being the best corrective internal tide model. As can be seen from the variance reduction maps (Figure 11a to c), the three models reduce variance (blue color) in the parts of the swath where the coherent internal tide signal is strong enough (Figure 10). Outside these areas, the internal tide models tend to add variance, and the variance reductions become positive. This undesirable effect of the correction models is mainly observed in the central part of the swath (area 2), where the higher modes contribute significantly to the SLA variability (see Figure 4). The effect in area 2 is pronounced for ITkars_p1 (Figure 11b), indicating a prediction failure. When considering the independent SLA_pca_L2 data (period 2, Table 3), HRET removes 21% of the variance. For ITkars_p1 and ITkars_pca_p1, the variance is reduced by 45% and 55% respectively. The impact of PCA on the derivation of the M2 internal tide atlas is highlighted here by the 10% gap between the percentages of variance reduction when applying the two models based on SWOT observations. The variance reduction figures confirm that the correction works better on SLA_pca_L2 (Figure 11 d to e). Although there are still swath locations with positive variance reduction, this is no longer concentrated in the central part. Variance reductions are dominated by negative values for ITkars_p1 (Figure 11e) and ITkars_pca_p1 (Figure 11f).

Table3: Comparative table of standard deviations (cm) of SLA and SLA_pca_L2 detided with either M2 HRET, M2 ITkars or M2 ITkars_pca models over period 1 (from late March to early June 2023, the first 70 cycles) and period 2 (from early June to early July 2023, the last 34 cycles). ITkars_p1 and ITkar_pca_p1 models were built on period 1 and validated on period 2. The ratio between detided SLA and total SLA is indicated in the parentheses (in percent).

	Period 1		Period 2	
	SLA	SLA_pca_L2	SLA	SLA_pca_L2
no IT correction	2.56	1.33	2.79	1.15
HRET	2.39 (93%)	0.99 (74%)	2.64 (95%)	0.91 (79%)
ITkars_p1	2.18 (85%)	0.53 (40%)	2.65 (95%)	0.63 (55%)
ITkars_pca_p1	2.21 (86%)	0.42 (32%)	2.55 (91%)	0.52 (45%)

433

434
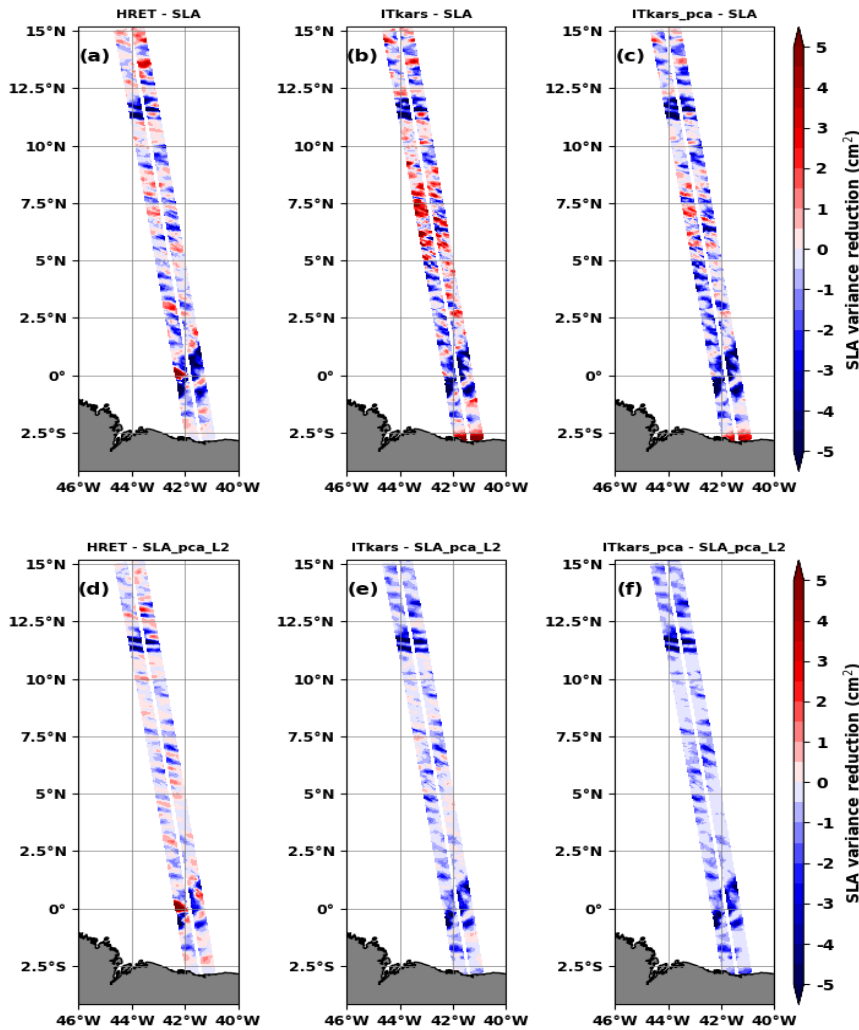
Figure 11: Variance reduction (in cm²) on period 2 from early June to early July (last 34 cycles) when using either M2 HRET (left column) or M2 ITkars_p1 (middle column) or M2 ITkars_pca_p1 (right column) to correct the total SLA (top line) or SLA_pca_L2 (bottom line).

438

439

4- Discussion and perspectives

In this study, we explored and characterized the internal tide signal in SWOT KaRIn observations over the Cal/Val period (1-day orbit) between late March and early July 2023 (104 cycles) and along the track 20 located off the Amazon shelf in the tropical Atlantic between 2°S and 15°N. The internal tide

as seen by SWOT is a mixture of several spatial scales, including baroclinic modes 1 and 2 defined by wavelengths between 180-90 km and 80-60 km respectively. SWOT also sees very intense fine-scale structures (wavelengths between 50-2 km) that we have associated with higher baroclinic modes, including modes 3, 4 and 5 according to Barbot et al., (2021). As a result, SWOT seems to live up to expectations, providing a direct 2D view of the internal tide sea surface signatures and even access to smaller scales.

Our approach to extract the internal tide signal through the 1-day SWOT data consisted firstly of filtering the large scale (including the mesoscale) by subtracting the DUACS MSLA from the SWOT observations; then we reintroduced the internal tide correction HRET from Zaron (2019) to obtain a SLA consisting of the total internal tide signal. We either performed the harmonic analysis (as in section 2) or proceeded upstream to the PCA before the harmonic analysis (as in section 3). The internal tide model based on harmonic analysis of SWOT KaRin data was referenced ITkars (Internal Tide from KaRin Swot), the one obtained by combining PCA and harmonic analysis ITkars_pca. We focused on the semi-diurnal frequencies M2, S2 and N2.

Spatial patterns of M2 internal tides from ITkars and ITkars_pca models agreed with the M2 HRET model based on nearly 25 years of conventional altimeter (nadir) observations. The similarities between models based on SWOT Karin and model with conventional altimeter are partly linked to the fact that SWOT data are analyzed over March to July during which the internal tide is most stable and coherent off the Amazon shelf (Tchilibou et al., 2022). One consequence of analyzing SWOT data over this short 104-day window is that the amplitude of the internal tide is stronger with SWOT estimation than with HRET. This result is logical since the intensity of the coherent internal tide depends on the length of the time series analyzed: a longer time series allows a better estimate of the coherent signal which is therefore smoother (Ansong et al.,2015; Zhou et al.,2015; Nash et al.,2012). The separation of M2 from O1 is not ensured with 104 cycles of SWOT 1-day data, however, in this region the amplitude of the internal tide is negligible at O1 frequency compared to M2 (see Figure 1 in Tchilibou et al.,2022), so M2 ITkars_pca is thus quite reliable.

The maps of N2 and S2 highlight the contamination of ITkars by signals other than the coherent internal tide, and particularly by very small scales. We hypothesize that the contamination is due to the leakage of nonlinear waves, incoherent internal tides, and ocean variability in the harmonic analyses. Regarding ocean variability, part of it is not captured by DUACS and was therefore not subtracted from the SLA. Moreover, subtracting the mesoscale, as we have done, is itself a possible source of error in estimating the internal tide (Zaron and Ray, 2018). One way to reduce the effects of contamination by ocean circulation would be to apply a simultaneous internal tide and mesoscale inversion method as proposed by Ubelmann et al. (2022). The combination of PCA and harmonic analysis gives semi-diurnal ITkars_pca maps (M2, S2 and N2) with similar patterns. The amplitude of N2 ITkars_pca deduced from SWOT is of the same order as that in the new product HRET14 (Zaron and Elipot 2024). The result is encouraging for S2, especially as the length of the 1-day observations is not sufficient to correctly separate it from waves such as Sa and Ssa, whose periods are identical to those of the annual and semi-annual variation of the ocean. A longer time series is needed to better separate the internal tide components from SWOT observation, and we will consider analyses of the 21-day SWOT science orbit data when the time series will be long enough.

PCA has improved our estimate of the internal tide model from the SWOT KaRin data. From the PCA we kept the first two main modes (PCA1 and PCA2) and considered them as the coherent internal tide given their fairly stationary character. Thus, the coherent internal tide accounts for 21.42% (12.3 of PCA1 and 9.12 of PCA2) of SLA variance in 1-day SWOT observations, a proportion in line with the studies of Zaron (2017) and Egbert and Erofeeva (2021) in this region. The coherent internal tide

isolated through the PCA consists of mode1, mode 2 noticeable in PCA1 and PCA2. The fact that the coherent internal tide signal is projected onto two main modes of the PCA is an open question. The principal components of PCA1 and PCA2 are shifted by 3 to 4 days, about a quarter of the aliased frequency of M2, which could correspond to a phase quadrature, as there is between the imaginary and real parts needed to reconstruct a sinusoidal signal. Instead of being the real and imaginary parts of a signal, PCA1 and PCA2 could also represent the same phenomenon and highlight its evolution in area 2 in the middle of the swaths: the moderation of internal tides in area 2 with PCA1 and their intensification with PCA2. This type of PCA/EOF behavior is observed in the case of ENSO studies in the Pacific (Takahashi et al., 2011). The peaks on the wave number spectrum of PCA1 and PCA2 are shifted by few kilometers at the mode 1 and mode 2 scales, suggesting a change in wavelengths relating to changes in stratification conditions as suggested by Barbot et al. (2021). A longer series of Cal/Val observations could have helped to better distinguish PCA1 from PCA2.

The principal components (time series) of PCA1 and PCA2 provide an overview and an opportunity to study the daily variability of internal tide amplitude, a perspective difficult to access with conventional altimetry missions. This opportunity to learn more about the temporal variability of the internal tide using a single high-resolution mission is lost, or at least postponed, with SWOT's switch to its 21-days scientific orbit. One of the limitations of using PCA to analyze SWOT data is probably its sensitivity to track length. The total variance is distributed differently in the principal components depending on whether the track is long or short, or whether ocean dynamics change significantly along the track. It would be interesting to look at this point in the perspective of a global model, for example. We are curious to know how the PCA will behave in the case of multi-track use, and at their crossing points.

In the context of 1-day SWOT observations, the use of PCA can be useful in determining wave frequencies of interest for the development of the coherent internal tide model. The combination of PCA and harmonic analysis further reveals the observational potential of SWOT. We are currently working on other SWOT tracks in various ocean regions to test the robustness of our method combining PCA and harmonic analysis. We also plan to explore in situ observations of the SWOT Cal/Val and other databases to understand better our results. Work remains to be done to confirm the presence of mode 3 in the coherent internal tide signal in this region. The incoherence of the internal tide and its interaction with the circulation are other issues to be addressed with these SWOT data.

The final issue addressed in this study was the correction of the internal tide signal in the SWOT 1-day observations. On average, the HRET model corrects only 6% of the SLA variance over the Cal/Val period, while ITkars based on SWOT observations corrects 12% (Table 2). These percentages are low due to the high degree of internal tides incoherency in this part of the ocean. However, they indicate that the HRET correction is not efficient enough. It would be more relevant to directly evaluate the internal tide signals on 1-day SWOT observations and then use it as a correction model. The harmonic analysis may be sufficient if the aim is to apply the tidal model to the same data, but if not, the previous step of the PCA is recommended to obtain a more realistic model. The question of correcting internal tides and improving internal tide models will also remain a challenge for the exploitation of SWOT's 21-day cycles.

Authors contributions: This work is part of the Marée - SWOT project funded by the CNES at CLS. MT's work and analyses are supervised by LC and FL. Conceptualization: TM, LC, FL, CU. MT wrote the paper with contributions from all co-authors.

534 **Competing interests:** The contact author has declared that none of the authors has any
535 competing interests
536
537 **References:**

538 Aguedjou, H. M. A., Dadou, I., Chaigneau, A., Morel, Y., and Alory, G.: Eddies in the Tropical Atlantic
539 Ocean and Their Seasonal Variability, Geophysical Research Letters, 46, 12156–12164,
540 https://doi.org/10.1029/2019GL083925, 2019.

541 Alford, M. H., Peacock, T., MacKinnon, J. A., Nash, J. D., Buijsman, M. C., Centurioni, L. R., Chao, S.-Y.,
542 Chang, M.-H., Farmer, D. M., Fringer, O. B., Fu, K.-H., Gallacher, P. C., Graber, H. C., Helfrich, K. R.,
543 Jachec, S. M., Jackson, C. R., Klymak, J. M., Ko, D. S., Jan, S., Johnston, T. M. S., Legg, S., Lee, I.-H., Lien,
544 R.-C., Mercier, M. J., Moum, J. N., Musgrave, R., Park, J.-H., Pickering, A. I., Pinkel, R., Rainville, L., Ramp,
545 S. R., Rudnick, D. L., Sarkar, S., Scotti, A., Simmons, H. L., St Laurent, L. C., Venayagamoorthy, S. K.,
546 Wang, Y.-H., Wang, J., Yang, Y. J., Paluszkiewicz, T., and (David) Tang, T.-Y.: The formation and fate of
547 internal waves in the South China Sea, Nature, 521, 65–69, https://doi.org/10.1038/nature14399,
548 2015.

549 Ansong, J. K., Arbic, B. K., Buijsman, M. C., Richman, J. G., Shriver, J. F., and Wallcraft, A. J.: Indirect
550 evidence for substantial damping of low-mode internal tides in the open ocean, JGR Oceans, 120,
551 6057–6071, https://doi.org/10.1002/2015JC010998, 2015.

552 Arbic, B., Richman, J., Shriver, J., Timko, P., Metzger, J., and Wallcraft, A.: Global Modeling of Internal
553 Tides Within an Eddying Ocean General Circulation Model, oceanog, 25, 20–29,
554 https://doi.org/10.5670/oceanog.2012.38, 2012.

555 Assene, F., Koch-Larrouy, A., Dadou, I., Tchilibou, M., Morvan, G., Chanut, J., Costa Da Silva, A.,
556 Vantrepotte, V., Allain, D., and Tran, T.-K.: Internal tides off the Amazon shelf – Part 1: The importance
557 of the structuring of ocean temperature during two contrasted seasons, Ocean Sci., 20, 43–67,
558 https://doi.org/10.5194/os-20-43-2024, 2024.

559 Bai, X., Lamb, K. G., and Da Silva, J. C. B.: Small-Scale Topographic Effects on the Generation of Along-
560 Shelf Propagating Internal Solitary Waves on the Amazon Shelf, JGR Oceans, 126, e2021JC017252,
561 https://doi.org/10.1029/2021JC017252, 2021.

562 Ballarotta, M., Ubelmann, C., Veillard, P., Prandi, P., Etienne, H., Mulet, S., Faugère, Y., Dibarboure, G.,
563 Morrow, R., and Picot, N.: Improved global sea surface height and current maps from remote sensing
564 and in situ observations, Earth Syst. Sci. Data, 15, 295–315, https://doi.org/10.5194/essd-15-295-2023,
565 2023.

566 Ballarotta, M., Ubelmann, C., Pujol, M.-I., Taburet, G., Fournier, F., Legeais, J.-F., Faugère, Y.,
567 Delepoulle, A., Chelton, D., Dibarboure, G., and Picot, N.: On the resolutions of ocean altimetry maps,
568 Ocean Sci., 15, 1091–1109, https://doi.org/10.5194/os-15-1091-2019, 2019.

569 Barbot, S., Lyard, F., Tchilibou, M., and Carrere, L.: Background stratification impacts on internal tide
570 generation and abyssal propagation in the western equatorial Atlantic and the Bay of Biscay, Ocean
571 Sci., 17, 1563–1583, https://doi.org/10.5194/os-17-1563-2021, 2021.

572 Brandt, P., Rubino, A., and Fischer, J.: Large-Amplitude Internal Solitary Waves in the North Equatorial
573 Countercurrent, J. Phys. Oceanogr., 32, 1567–1573, https://doi.org/10.1175/1520-
574 0485(2002)032<1567:LAISWI>2.0.CO;2, 2002.

575 Buijsman, M. C., Arbic, B. K., Richman, J. G., Shriver, J. F., Wallcraft, A. J., and Zamudio, L.: Semidiurnal

576 internal tide incoherence in the equatorial Pacific, JGR Oceans, 122, 5286–5305,
577 https://doi.org/10.1002/2016JC012590, 2017.

578 Carrere, L., Arbic, B. K., Dushaw, B., Egbert, G., Erofeeva, S., Lyard, F., Ray, R. D., Ubelmann, C., Zaron,
579 E., Zhao, Z., Shriver, J. F., Buijsman, M. C., and Picot, N.: Accuracy assessment of global internal-tide
580 models using satellite altimetry, Ocean Sci., 17, 147–180, https://doi.org/10.5194/os-17-147-2021,
581 2021.

582 Chelton, D. B., Schlax, M. G., and Samelson, R. M.: Global observations of nonlinear mesoscale eddies,
583 Progress in Oceanography, 91, 167–216, https://doi.org/10.1016/j.pocean.2011.01.002, 2011.

584 De Macedo, C. R., Koch-Larrouy, A., Da Silva, J. C. B., Magalhães, J. M., Lentini, C. A. D., Tran, T. K., Rosa,
585 M. C. B., and Vantrepotte, V.: Spatial and temporal variability in mode-1 and mode-2 internal solitary
586 waves from MODIS-Terra sun glint off the Amazon shelf, Ocean Sci., 19, 1357–1374,
587 https://doi.org/10.5194/os-19-1357-2023, 2023.

588 Dibarboure, G., Anadon, C., Briol, F., Cadier, E., Chevrier, R., Delepoulle, A., Faugère, Y., Laloue, A.,
589 Morrow, R., Picot, N., Prandi, P., Pujol, M.-I., Raynal, M., Treboutte, A., and Ubelmann, C.: Blending 2D
590 topography images from SWOT into the altimeter constellation with the Level-3 multi-mission DUACS
591 system, EGUsphere [preprint], https://doi.org/10.5194/egusphere-2024-1501, 2024.

592 Duda, T. F., Lin, Y.-T., Buijsman, M., and Newhall, A. E.: Internal Tidal Modal Ray Refraction and Energy
593 Ducting in Baroclinic Gulf Stream Currents, Journal of Physical Oceanography, 48, 1969–1993,
594 https://doi.org/10.1175/JPO-D-18-0031.1, 2018.

595 Dufau, C., Orsztynowicz, M., Dibarboure, G., Morrow, R., and Le Traon, P.: Mesoscale resolution
596 capability of altimetry: Present and future, JGR Oceans, 121, 4910–4927,
597 https://doi.org/10.1002/2015JC010904, 2016.

598 Dunphy, M. and Lamb, K. G.: Focusing and vertical mode scattering of the first mode internal tide by
599 mesoscale eddy interaction, JGR Oceans, 119, 523–536, https://doi.org/10.1002/2013JC009293, 2014.

600 Dunphy, M., Ponte, A. L., Klein, P., and Le Gentil, S.: Low-Mode Internal Tide Propagation in a Turbulent
601 Eddy Field, Journal of Physical Oceanography, 47, 649–665, https://doi.org/10.1175/JPO-D-16-0099.1,
602 2017.

603 Dushaw,B. D: An Empirical Model for Mode-1 Internal Tides Derived from Satellite Altimetry:
604 Computing Accurate Tidal Predictions at Arbitrary Points over the World oceans, Technical
605 Memorandum APL-UW TM: https://apl.uw.edu/project/project.php?id=tm_1-15, (last access: 2 June
606 2024), 2015.

607 Egbert, G. D. and Erofeeva, S. Y.: An Approach to Empirical Mapping of Incoherent Internal Tides With
608 Altimetry Data, Geophysical Research Letters, 48, e2021GL095863,
609 https://doi.org/10.1029/2021GL095863, 2021.

610 Fu, L.-L. and Ubelmann, C.: On the Transition from Profile Altimeter to Swath Altimeter for Observing
611 Global Ocean Surface Topography, Journal of Atmospheric and Oceanic Technology, 31, 560–568,
612 https://doi.org/10.1175/JTECH-D-13-00109.1, 2014.

613 Fu, L.-L., Alsdorf, D., Rodriguez, E., Morrow, R., Mognard, N., Lambin, J., Vaze, P., and Lafon, T.: THE
614 SURFACE WATER AND OCEAN TOPOGRAPHY (SWOT) MISSION, California, CA: JPL publication, 2012.

615 Gill, A. E.: Atmosphere-ocean dynamics, Nachdr., Acad. Press, San Diego, 662 pp., 2006.

616   Jackson, C., Da Silva, J., and Jeans, G.: The Generation of Nonlinear Internal Waves, oceanog, 25, 108–
617   123, https://doi.org/10.5670/oceanog.2012.46, 2012.

618   Jolliffe, I. T.: Principal Component Analysis, Springer New York, New York, NY,
619   https://doi.org/10.1007/978-1-4757-1904-8, 1986.

620   Kelly, S. M.: The Vertical Mode Decomposition of Surface and Internal Tides in the Presence of a Free
621   Surface and Arbitrary Topography, Journal of Physical Oceanography, 46, 3777–3788,
622   https://doi.org/10.1175/JPO-D-16-0131.1, 2016.

623   Le Guillou, F., Lahaye, N., Ubelmann, C., Metref, S., Cosme, E., Ponte, A.: Joint estimation of balanced
624   motions and internal tides from future wide-swath altimetry. Journal of Advances in Modeling Earth
625   Systems, 13(12), e2021MS002613. https://doi.org/10.1029/2021ms002613, 2021.

626   Le Provost, C.: Chapter 6 Ocean Tides, in: International Geophysics, vol. 69, Elsevier, 267–303,
627   https://doi.org/10.1016/S0074-6142(01)80151-0, 2001.

628   Lentini, C., Magalhães, J., Da Silva, J., and Lorenzzetti, J.: Transcritical Flow and Generation of Internal
629   Solitary Waves off the Amazon River: Synthetic Aperture Radar Observations and Interpretation,
630   Oceanog., 29, 187–195, https://doi.org/10.5670/oceanog.2016.88, 2016.

631   Lyard, F. H., Allain, D. J., Cancet, M., Carrere, L., and Picot, N.: FES2014 global ocean tide atlas: design
632   and performance, Ocean Sci., 17, 615–649, https://doi.org/10.5194/os-17-615-2021, 2021.

633   Magalhaes, J. M., Da Silva, J. C. B., Buijsman, M. C., and Garcia, C. A. E.: Effect of the North Equatorial
634   Counter Current on the generation and propagation of internal solitary waves off the Amazon shelf
635   (SAR observations), Ocean Sci., 12, 243–255, https://doi.org/10.5194/os-12-243-2016, 2016.

636   Morrow, R., Fu, L.-L., Ardhuin, F., Benkiran, M., Chapron, B., Cosme, E., d'Ovidio, F., Farrar, J. T., Gille,
637   S. T., Lapeyre, G., Le Traon, P.-Y., Pascual, A., Ponte, A., Qiu, B., Rascle, N., Ubelmann, C., Wang, J., and
638   Zaron, E. D.: Global Observations of Fine-Scale Ocean Surface Topography With the Surface Water and
639   Ocean Topography (SWOT) Mission, Front. Mar. Sci., 6, 232,
640   https://doi.org/10.3389/fmars.2019.00232, 2019.

641   Nash, J., Shroyer, E., Kelly, S., Inall, M., Duda, T., Levine, M., Jones, N., and Musgrave, R.: Are Any
642   Coastal Internal Tides Predictable?, oceanog, 25, 80–95, https://doi.org/10.5670/oceanog.2012.44,
643   2012.

644   Nelson, A. D., Arbic, B. K., Zaron, E. D., Savage, A. C., Richman, J. G., Buijsman, M. C., and Shriver, J. F.:
645   Toward Realistic Nonstationarity of Semidiurnal Baroclinic Tides in a Hydrodynamic Model, JGR
646   Oceans, 124, 6632–6642, https://doi.org/10.1029/2018JC014737, 2019.

647   Niwa, Y. and Hibiya, T.: Estimation of baroclinic tide energy available for deep ocean mixing based on
648   three-dimensional global numerical simulations, J Oceanogr, 67, 493–502,
649   https://doi.org/10.1007/s10872-011-0052-1, 2011.

650   Ponte, A. L. and Klein, P.: Incoherent signature of internal tides on sea level in idealized numerical
651   simulations, Geophysical Research Letters, 42, 1520–1526, https://doi.org/10.1002/2014GL062583,
652   2015.

653   Ray, R. D. and Mitchum, G. T.: Surface manifestation of internal tides in the deep ocean: observations
654   from altimetry and island gauges, Progress in Oceanography, 40, 135–162,
655   https://doi.org/10.1016/S0079-6611(97)00025-6, 1997.

Savage, A. C., Waterhouse, A. F., and Kelly, S. M.: Internal Tide Nonstationarity and Wave–Mesoscale Interactions in the Tasman Sea, Journal of Physical Oceanography, 50, 2931–2951, https://doi.org/10.1175/JPO-D-19-0283.1, 2020.

Solano, M. S., Buijsman, M. C., Shriver, J. F., Magalhaes, J., Da Silva, J., Jackson, C., Arbic, B. K., and Barkan, R.: Nonlinear Internal Tides in a Realistically Forced Global Ocean Simulation, JGR Oceans, 128, e2023JC019913, https://doi.org/10.1029/2023JC019913, 2023.

St. Laurent, L. and Garrett, C.: The Role of Internal Tides in Mixing the Deep Ocean, J. Phys. Oceanogr., 32, 2882–2899, https://doi.org/10.1175/1520-0485(2002)032<2882:TROITI>2.0.CO;2, 2002.

Takahashi, K., Montecinos, A., Goubanova, K., and Dewitte, B.: ENSO regimes: Reinterpreting the canonical and Modoki El Niño: REINTERPRETING ENSO MODES, Geophys. Res. Lett., 38, n/a-n/a, https://doi.org/10.1029/2011GL047364, 2011.

Tchilibou, M., Gourdeau, L., Lyard, F., Morrow, R., Koch Larrouy, A., Allain, D., and Djath, B.: Internal tides in the Solomon Sea in contrasted ENSO conditions, Ocean Sci., 16, 615–635, https://doi.org/10.5194/os-16-615-2020, 2020.

Tchilibou, M., Koch-Larrouy, A., Barbot, S., Lyard, F., Morel, Y., Jouanno, J., and Morrow, R.: Internal tides off the Amazon shelf during two contrasted seasons: interactions with background circulation and SSH imprints, Ocean Sci., 18, 1591–1618, https://doi.org/10.5194/os-18-1591-2022, 2022.

Ubelmann, C., Dibarboure, G., Gaultier, L., Ponte, A., Ardhuin, F., Ballarotta, M., and Faugère, Y.: Reconstructing Ocean Surface Current Combining Altimetry and Future Spaceborne Doppler Data, JGR Oceans, 126, e2020JC016560, https://doi.org/10.1029/2020JC016560, 2021.

Ubelmann, C., Carrere, L., Durand, C., Dibarboure, G., Faugère, Y., Ballarotta, M., Briol, F., and Lyard, F.: Simultaneous estimation of ocean mesoscale and coherent internal tide sea surface height signatures from the global altimetry record, Ocean Sci., 18, 469–481, https://doi.org/10.5194/os-18-469-2022, 2022.

Ubelmann, C., P. Klein, and L.-L. Fu: Dynamic interpolation of sea surface height and potential applications for future high-resolution altimetry mapping. J. Atmos. Ocean. Technol., 32, 177–184, https://doi.org/10.1175/JTECH-D-14-00152.1, 2015

Vic, C., Naveira Garabato, A. C., Green, J. A. M., Waterhouse, A. F., Zhao, Z., Melet, A., De Lavergne, C., Buijsman, M. C., and Stephenson, G. R.: Deep-ocean mixing driven by small-scale internal tides, Nat Commun, 10, 2099, https://doi.org/10.1038/s41467-019-10149-5, 2019.

Wang, H., Grisouard, N., Salehipour, H., Nuz, A., Poon, M., & Ponte, A. L.: A deep learning approach to extract internal tides scattered by geostrophic turbulence. Geophysical Research Letters, 49, e2022GL099400. https://doi.org/10.1029/2022GL099400, 2022.

Wang, J. and Fu, L.-L.: On the Long-Wavelength Validation of the SWOT KaRIn Measurement, Journal of Atmospheric and Oceanic Technology, 36, 843–848, https://doi.org/10.1175/JTECH-D-18-0148.1, 2019.

Zaron E. D. and S. Elipot: Estimates of Baroclinic Tidal Sea Level and Currents from Lagrangian Drifters and Satellite Altimetry, Journal of Atmospheric and Oceanic Technology, 41, 781-802 https://doi.org/10.1175/JTECH-D-23-0159.1, 2024.

Zaron, E. D.: Mapping the nonstationary internal tide with satellite altimetry, JGR Oceans, 122, 539–

554, https://doi.org/10.1002/2016JC012487, 2017.

Zaron, E. D.: Baroclinic Tidal Sea Level from Exact-Repeat Mission Altimetry, Journal of Physical Oceanography, 49, 193–210, https://doi.org/10.1175/JPO-D-18-0127.1, 2019.

Zaron, E. D. and Ray, R. D.: Aliased Tidal Variability in Mesoscale Sea Level Anomaly Maps, Journal of Atmospheric and Oceanic Technology, 35, 2421–2435, https://doi.org/10.1175/JTECH-D-18-0089.1, 2018.

Zhao, Z.: Mapping Internal Tides from Satellite Altimetry Without Blind Directions, JGR Oceans, 124, 8605–8625, https://doi.org/10.1029/2019JC015507, 2019.

Zhao, Z.: Seasonal mode-1 M2 internal tides from satellite altimetry, Journal of Physical Oceanography, https://doi.org/10.1175/JPO-D-21-0001.1, 2021.

Zhou, X., Wang, D., and Chen, D.: Validating satellite altimeter measurements of internal tides with long-term TAO/TRITON buoy observations at 2°S–156°E, Geophysical Research Letters, 42, 4040–4046, https://doi.org/10.1002/2015GL063669, 2015.